

www.acsanm.org Article

Synthesis and Characterization of Amorphous Lawsone Polymer Dots for Fluorescent Applications

Jesus Hernandez, Alex Robb, Savannah Servera, Nanor Bedrosian, Osma Gomez, Zachary Duca, Michael B. Thomas, Daniel Tamae, Paula L. Fischhaber, Simon J. Garrett, Patrick A. Ward,* and Joseph A. Teprovich, Jr.*



Cite This: ACS Appl. Nano Mater. 2023, 6, 20639-20651



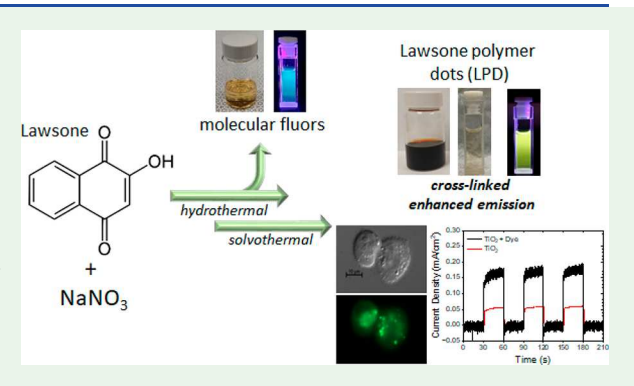
ACCESS

Metrics & More

Article Recommendations

supporting Information

ABSTRACT: In this work, a two-step hydrothermal/solvothermal process was developed to generate highly fluorescent lawsone polymer dots (LPDs) utilizing an inexpensive and abundant starting material, 2-hydroxy-1,4-napththoquinone (lawsone). This hydrothermal/solvothermal process produces LPDs that have excitation independent emission with well-defined electronic transitions. This two-step protocol provides a straightforward approach to remove unwanted small molecular fluorescence, which has plagued carbon dot systems, without the need for advanced chromatographic purification methods or steps. A series of spectroscopic, electrochemical, and theoretical experiments suggest that this process proceeds via a sequential dehydration and dehydrogenation pathway to cross-link the lawsone into a carbon dot structure. This polymerization process helps to stabilize and favor certain electronic



transitions inherently present in the lawsone monomer. The generation of the LPDs results in a 2 order of magnitude increase in the emission intensity and a quantum yield of 37%. This behavior is likely the result of the cross-linked structure shielding these electronic states from deactivation caused by nonradiative processes such as vibrational coupling and excited state quenching from thermal deactivation and solvent collisions. This finding is consistent with a cross-linked enhanced emission (CEE) mechanism, as previously observed for other similar systems. The LPDs were then incorporated into a TiO₂ photoanode and utilized as a photosensitizer in a dye-sensitized solar cell (DSSC) which showed an enhancement in photocurrent density over pure TiO₂. We also prepared a derivative of the LPDs utilizing a diethylene triamine additive (nitrogen-doped lawsone polymer dots (N-LPDs)) using the same two-step protocol and demonstrated its potential as a fluorescence microscopy dye for imaging MDA-MB-231 cancer cells.

KEYWORDS: carbon dot, lawsone, DFT, fluorescence microscopy dye, DSSC, cross-linked enhanced emission

1. INTRODUCTION

Carbon dots (CDs) were first discovered as byproducts during the synthesis and purification of single-walled carbon nanotubes reported by Xu et al. 2004. CDs are an emerging class of carbon nanomaterials that possess robust photostability, tunable emission wavelength, facile functionalization, good biocompatibility, and economical fabrication. Their unique photophysical properties have drawn attention due to their potential in biomedical and energy applications. Methods such as microwave assisted pyrolysis and hydrothermal/solvothermal synthesis are commonly used to prepare CDs from organic precursors. As this field has evolved, a series of subcategories of CDs have been developed and reported in the literature: graphene quantum dots (GQDs), 2,17-20 carbon quantum dots (CQDs), 3,21,22 and carbon polymer dots (CPDs). In general, GQDs and CQDs are classified as having a network composed of sp² carbons which form a graphitic lattice, display fluorescent properties that are size and

heteroatom/functional group dependent, and range in size from 2 to 10 nm. ¹⁰ On the other hand, CPDs are made up of an sp³ carbon network which typically lacks a well-defined graphitic carbon lattice, exhibit molecular-like fluorescence, and are larger than 10 nm. ²³ Although carbon dots are classified as GQDs/CQDs or CPDs, there is still no consensus or well-defined classification methodology. ^{17,25}

With respect to the larger class CPDs, they are typically prepared from a bottom-up approach in which an organic precursor undergoes multiple routes of dehydration, condensa-

Received: July 13, 2023
Revised: October 13, 2023
Accepted: October 19, 2023
Published: November 6, 2023





tion, polymerization, and carbonization via a hydrothermal/solvothermal route. In general, the structure of the resulting CPDs consists of an ordered fluorophore core surrounded by an amorphous polymer shell and chains. The photoluminescence properties of the CPDs are attributed to the trapping and stabilization of the fluorescent domain(s) within the amorphous polymeric shell. This trapping and these enhanced emissive properties are attributed to the cross-linked enhanced emission (CEE) effect. The CEE effect improves the luminescence of a material by decreasing vibrational and rotational motion, while increasing the desired radiative processes (i.e., fluorescence) inherently present in the organic precursor(s). The CEE effect is analogous to the use of a core—shell structure to protect and enhance the photoluminescent properties of perovskite nanoparticles.

To understand how the CEE effect improves fluorescence in CPDs, identifying the key chemical and structural features leading to this behavior would be highly desirable. This is a challenge because some of the reported CDs exhibit excitation dependent emission. Excitation dependent emission often results from the generation of small molecular fluor byproducts during the synthesis and/or multiple emission centers present in the CDs. These small molecular fluors often possess high quantum yields, blue emission, and excitation dependent emission.^{31–33} As a result, the photophysical properties of many CD systems have come under deep scrutiny with the finding that they might be due to the photophysical properties of small molecule fluors and not the CDs. Additionally, the "quantum confinement" model proposed as the mechanism of fluorescence claimed for certain systems is also under scrutiny since the role and interplay between graphitic cores and surface states/functional groups is poorly understood.³⁴ Through careful analysis of the resulting CD product solution, a number of fluors have been identified: 5-oxo-1,2,3,5-tetrahydroimidazo [1,2- α] pyridine-7-carboxylic acid (IPCA),³⁵ [3,2- α] pyridine-7carboxylic acid (TPCA),³⁶ and N-(2-hydroxyethyl)-2-oxo-1vinyl-6-(vinylamino)-1,2-dihydropyridine-4-carboxamide (NVDPA).³⁷ In an effort to address this issue, the work of Baker determined that common practices of purification such as high speed centrifugation, syringe filtering, or dialysis through semipermeable membranes are not adequate approaches for removing the contribution of the problematic molecular fluors.33 This work suggests that techniques such as HPLC or column chromatography are likely the most adequate approaches to minimize or limit the contribution of molecular fluors in carbon dot systems. $^{14,38-40}$ Although these purification approaches are highly effective, it would be desirable to develop a synthetic approach that could effectively minimize or eliminate molecular fluorescence without the need for time intensive separation techniques.

Herein, we report the synthesis of large CDs from the sustainable, plant based organic precursor lawsone (2-hydroxy-1,4-napththoquinone), which exhibits well-defined molecular-like emission that can potentially be used as a model to study the CEE effect. The two step hydrothermal/solvothermal protocol developed in this work provides a chromatography free approach to mitigate the contribution of molecular fluors to the photophysical properties of the LPDs. By leveraging the CEE approach to stabilize and enhance the emission from a fluorophore based on lawsone, it may be possible to more effectively study its photophysical properties. The synthesis of lawsone polymer dots (LPDs) was optimized, displaying an emission maximum at 527 nm in a quantum yield of 37%. A

series of spectroscopic techniques was utilized to identify key structural features of the fluorophore(s) that could be responsible for the observed photophysical properties. From this analysis, two possible lawsone based fluorophore structures are proposed and their UV-vis, FTIR, and electronic transitions were calculated via time dependent-density functional theory (TD-DFT). The LPDs were then infused into a mesoporous TiO₂ film and utilized a photosensitizer in a dye-sensitized solar cell (DSSC). A clear enhancement in the photocurrent was observed for the DSSC containing the LPD dye over the baseline of a pure TiO2 photosensitizer without any added dye. The LPDs were then modified via a diethylenediamine to prepare nitrogen-doped lawsone polymer dots (N-LPDs) which improved their water solubility and biocompatibility compared to the base LPDs. The N-LPDs were then successfully utilized as a fluorescence microscopy dye to image the MDA-MB-231 triple negative breast cancer cell line.

2. EXPERIMENTAL SECTION

2.1. Materials. 2-Hydroxy-1,4-napthoquinone, absolute ethanol, diethylene triamine, and sodium nitrate were purchased from Fisher Scientific and used as received.

2.2. Synthesis of Lawsone Polymer Dots (LPDs). The synthesis of lawsone polymer dots (LPDs) was adapted and modified from a previously utilized solvothermal approach in which they used 1,3dihydroxynapthalene and KIO₄ to synthesize red emissive carbon dots. 42 The LPDs in this study were prepared via solvothermal synthesis using a 50 mL autoclave reactor. A 50 mL Teflon liner vessel containing a magnetic stir bar, 10.00 g of DI water, 100.0 mg of lawsone, and 73.2 mg of sodium nitrate was prepared and then sonicated for 5 min. The Teflon liner was sealed within the autoclave reactor and wrapped with BrisketHeat heat tape and aluminum foil. A proportional-integralderivative (PID) temperature controller was used to heat the autoclave reactor from 120 to 210 °C at a ramp rate of 3 °C/min. The reaction was held at 210 °C for 24 h with continuous mixing. Afterward, the autoclave reactor was cooled to room temperature. Excess water was removed, and the remaining LPDs were rinsed three times with DI water. To the precursor LPDs, 10 g of ethanol was added, and the mixture was sonicated for 5 min. The reaction vessel was sealed and heated following the previous procedure but varying the amount of time the spent at 210 °C. Post-heating, the mixture was sonicated for 5 min and filtered through a 0.22 μm syringe filter. The nitrogen-doped lawsone polymer dots (N-LPDs) were prepared in a similar fashion except that 0.120 g of diethylene triamine was added to the reaction mixture. For the N-LPDs, the hydrothermal step of the synthesis was performed at 210 °C for 24 h, while the solvothermal step was performed at 210 °C for 1 h. The resulting N-LPD solution was then freeze-dried, and the resulting powder was dispersed in water.

2.3. Spectroscopic Characterization. The absorption spectra of the samples were measured and recorded with an Agilent Technologies Cary 60 UV-vis spectrophotometer. The excitation-emission maps, excitation spectra, emission spectra, and fluorescent lifetimes were measured using an Edinburgh Instruments Spectrofluorometer FS5 with a standard cuvette holder (SC-5). An EPL-375 ps pulsed laser with a wavelength of 375 ± 10 nm and a maximum average power of 5 mW was used to measure the fluorescent lifetimes. The quantum yields were measured by using the integrating sphere holder (SC-30) component of the spectrofluorometer. To measure the quantum yield and fluorescent lifetime of the sample without the inner filter effect, the absorbance of the excitation wavelength maximum was adjusted to 0.095-0.100. All samples were in a quartz cuvette with a path length of 10 mm and dissolved in either ethanol or water. The IR spectra of the samples were measured in the solid state and recorded using a PerkinElmer Spectrum 100 Fourier-Transform Infrared Spectrometer. The proton and carbon NMR spectrum of the samples were measured in DMSO-d₆ and recorded with a Bruker Advance III 400 MHz NMR spectrometer. The hydrodynamic radius of the LPDs was measured in 10 mM KNO₃ and recorded with a Brookhaven NanoBrook Omni Nanoparticle Analyzer.

Images of the LPDs on a lacey carbon copper grid were obtained with a ThermoFisher Talos F200C transmission electron microscope and Velox software. Then, ImageJ image processing software was used to determine the radius of the LPDs.

Femtosecond transient absorption spectroscopy experiments were performed using an ultrafast femtosecond laser source (Astrella) by Coherent incorporating a diode-pumped, mode-locked titanium sapphire laser (Vitesse), and a diode-pumped intracavity doubled Nd:YLF laser (Evolution) to generate a compressed laser output of 5.6 W. For optical detection, a Helios Fire transient absorption spectrometer coupled with an optical parametric amplifier (OPA), both provided by Ultrafast Systems LLC, was used. The sources of the pump and probe pulses were derived from the fundamental output of the Astrella (compressed output of 5.6 W, pulse width of 100 fs, repetition rate of 1 kHz, and center wavelength of 800 nm). Data analysis was performed with Surface Xplorer software supplied by Ultrafast Systems LLC. All measurements were conducted in degassed solutions at 298 K with sample rastering to prevent potential sample decomposition.

X-ray photoelectron spectroscopy (XPS) was performed using a Physical Electronics 5200 system equipped with non-monochromated Mg anode (1253.6 eV) operated at 100-300 W power and a 150 mm radius hemispherical analyzer with a single channeltron detector. Survey spectra (0–1000 eV binding energy) were collected using a pass energy of 178 eV with a 1.0 eV step size. Individual regions were collected with a pass energy of 45 eV with a 0.1 eV step size. The takeoff angle was 45° from the surface normal, and the analyzer was set for an analysis area of 6 mm × 6 mm. Charging of the samples was minimal (<1 eV), and calibration of the spectra was accomplished by assigning the largest C 1s photoemission peak as 284.6 eV. Powdered samples were pressed into indium foil, mounted onto a 25 mm diameter stainless steel sample holder using double-sided conductive tape, and measured without further treatment. Curve fitting was accomplished after X-ray satellite and Shirley background removal by using AugerScan software (RBD Instruments), using a common full-width at half-maximum and shape (% Gaussian/% Lorentzian) for each region but allowing intensity and binding energy for each peak to vary freely.

2.4. Theoretical Calculations. All computational calculations were carried out with Gaussian 09 software. First, geometry optimization of Fluorophore A and Fluorophore B was performed in the singlet ground state using the hybrid density functional theory (DFT) model B3LYP (Becke, 3-parameter, Lee—Yang—Parr) and 6-31G(d) basis set. Frequencies were calculated for Fluorophores A and B in their optimized geometry state. Then, linear response TD-DFT calculations were done using the theory and basis set to calculate the first 20 excited states with the solvent effect (ethanol). Output files were processed using the Gabedit graphical user interface software package to create the FT-IR and UV—vis spectra.

2.5. Cytotoxicity Evaluation. MDA-MB-231 triple negative breast cancer cells (ATCC) were treated with the lawsone based polymer dots at 10, 50, 100, 200, and 500 μ g/mL. DMSO was used to disperse the lawsone based polymer dots into media for a final concentration of 0.05% DMSO. The control (0 μ g/mL) cells were treated only with the same volume of DMSO used to introduce the lawsone based polymer dots into the media. The cells (3950 cells/well) were incubated with the lawsone based polymer dots at the different concentrations in DMEM (Dulbecco's Modified Eagle Medium) medium supplemented with 10% fetal bovine serum (FBS) in a 96-well plate for 48 h. Then, cells were treated with an MTT Cell Proliferation assay Kit (Cayman Chemical Company). A SpectraMax iD-3-2301 multimode microplate reader was used to take absorbance of each well at 570 and 630 nm. Cell viability was determined by eq 2.1, and the results were plotted using Origin graphing software.

% cell viability =
$$\frac{(Abs_{570 \text{ nm}} - Abs_{630 \text{ nm}})}{Abs_{control \text{ ave}}} \times 100$$
 (2.1)

2.6. Fluorescence Microscopy. MDA-MB-231 triple negative breast cancer cells (ATCC) were used for fluorescence imaging. The cells (40 000 cells/well in a 12-well plate) were incubated with

diethylenetriamine—lawsone polymer dots at a concentration of $10\,\mu\mathrm{g/mL}$ in Dulbecco's Modified Eagle Medium (DMEM) supplemented with 10% FBS in a 6-well plate for 24 h. After 24 h, DMEM was removed, and the cells were rinsed three times with phosphate buffered saline (PBS) solution. Then, a cell scraper was used to mechanically detach the cells from the bottom of the plate, resuspending the cells in $100\,\mu\mathrm{L}$ of PBS. The mixture containing the cells was then transferred onto a microscope slide and covered with a coverslip. A Zeiss Imager M2 with a Hamamatsu ORCA Flash 4.0 camera and a Zeiss 38 HE GFP filter set were used to take images of the cells at $10\times$ and $100\times$ (1.46 NA) magnification. The exposure time for the differential interference contrast (DIC) images was 150 ms. The exposure time for the GFP images was 80 ms. Acquisition and processing of images were done with ZEN Microscopy software V 3.4.

2.7. Cyclic Voltammetry. Cyclic voltammetry (CV) experiments were performed by using a BioLogic SP-300 potentiostat. A 3 mm diameter glassy carbon electrode was used as the working electrode with a platinum disk electrode as the counter electrode and pseudoreference. The voltammograms were internally referenced by the addition of ferrocene after the initial measurements. Experiments were performed in acetonitrile (MeCN).

2.8. DSSC Preparation. A 1:1 ethanol:water (EtOH:H₂O) solution containing 20 wt % TiO₂ nanoparticles (21 nm diameter) (Sigma) and 3 wt % acetic acid was prepared and mixed with an equal volume of an ethanol solution containing 10 wt % polyvinyl acetate (PVA, 10 000 mw) (Sigma). This TiO₂ and polymer suspension was then stirred for 24 h to achieve homogeneity. Fluorine doped tin oxide (FTO) glass substrates (Sigma) were cleaned via bath sonication. The glass substrates were sonicated in 3 M nitric acid, DI water, and acetone for 30 min each and then ozone treated under intense UV irradiation. Mesoporous TiO₂ nanoparticle films (1 cm wide) were then produced on FTO glass via doctor blading (one layer of Scotch brand tape thick). The bladed TiO₂ films were then dried in air and subsequently sintered in a box furnace at 500 °C for 1 h to produce mesoporous TiO₂ films. These films were then cut into 2×1.5 cm strips with 1 cm² active areas. TiO2-LPD films were prepared via soaking the TiO2 films in a concentrated solution of LPDs in EtOH for 24 h, followed by rinsing with MeOH and drying under a stream of air. The functionalized TiO₂ films (TiO₂-LPDs) on FTO glass (2 \times 1.5 cm) served as the photoanode component of the devices. Platinum coated FTO glass served as the cathode and was prepared by cutting precleaned FTO glass into 2 \times 2 cm slides and then depositing 75 μ L of a 4 mM H₂PtCl₆ solution (in EtOH) via drop-casting onto the slide and subsequently heating at 400 °C for 15 min. The liquid electrolyte used was an iodide/ tri-iodide redox couple (in ethylene glycol) and had the following composition: 0.1 M 1-butyl-3-methylimidazolium iodide (BMII), 0.01 M I₂, and 0.1 M 4-tert-butylpyridine (TBP). Dye-sensitized solar cells were produced in a sandwich cell architecture in which the photoanode and cathode and were clamped together with a 1 mm thick rubber spacer in-between. This rubber spacer contains a 1 × 1 cm square cutout that, when sandwiched between the anode and the cathode, creates a compartment for the electrolyte.

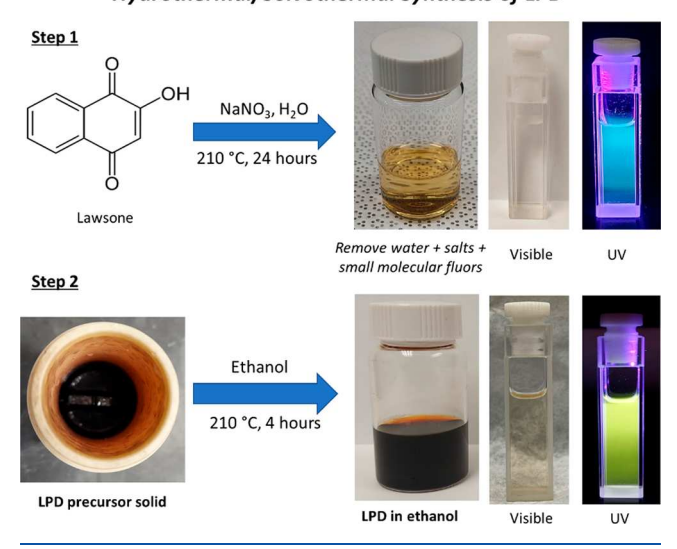
3. RESULTS AND DISCUSSION

3.1. Hydrothermal/Solvothermal Synthesis of LPDs.

The motivation for this work is to develop a synthetic method that can readily eliminate the small molecular fluor contaminants and isolate lawsone polymer dots (LPDs). This is expected to enable identification of key chemical and structural features that could provide additional insight into the CEE effect in this and similar systems. To address this, we utilized a two-step hydrothermal/solvothermal protocol for the synthesis of a CD from a lawsone organic source and a NaNO₃ oxidant. The hydrothermal/solvothermal process and isolation of the LPDs are outlined in Scheme 1. This dehydration and dehydrogenation synthesis and isolation process was tailored to maintain some of the structural features and inherent emissive states of lawsone. The first hydrothermal step produces the lawsone

Scheme 1. Hydrothermal/Solvothermal Synthesis of LPDs and Separation of Molecular Fluorophores

Hydrothermal/Solvothermal Synthesis of LPD



based LPD precursor along with small molecular fluor impurities in the presence of NaNO₃ in water. The resulting LPD precursor is hydrophobic and phase separates from the aqueous solution, leaving the salts and molecular fluor impurities in the aqueous solution. These impurities are then simply extracted by washing with water to eliminate the need for further separation (i.e., column chromatography). As shown in Scheme 1 and Figure S1, this aqueous fraction has the characteristic blue emission synonymous with the presence of small molecular fluors. To resuspend the LPDs, a second solvothermal process using pure ethanol was performed. This resulted in the production of a dark red-brown solution of the LPDs that was utilized for subsequent spectroscopic analysis. The synthetic method was optimized by evaluating a series of temperatures and times for each step, using the quantum yield of the LPDs as the screening parameter. This optimization indicated that the first step (hydrothermal) should be performed at 210 °C for 24 h, while the second step (solvothermal) should be performed at 210 °C for 4 h, which resulted in LPDs with a quantum yield of 37% (Figure S2). The fluorescence lifetime of the LPDs was obtained (Figure S3), and it exhibited a single exponential decay with an excited state lifetime of 5.1 ns. Many CD systems in the literature show

multiexponential decay, indicating a mixture of multiple fluorophores, which may be due to the molecular fluor impurities or various emissive states present in their final product. The single exponential decay suggests that there is a well-defined fluorophore present in the LPD structure.

3.2. Spectroscopic Analysis. The absorption, excitation, and emission spectra of the precursor, molecular lawsone, are compared to those of the product LPDs as shown in Figures 1a and S4a, utilizing the optimized conditions described in Scheme 1. Lawsone has an absorbance maximum at 330 nm which is attributed to the $\pi \to \pi^*$ transitions in the C=C regions present in the benzenoid ring. 43,44 After formation of the LPDs, we observed a significant reduction of the transition present at 330 nm and the formation of peaks at 450, 480, and 515 nm in the UV-vis spectrum. Interestingly, these peaks are also present in the excitation spectra of pure lawsone and LPDs. This behavior could be attributed to the dimerization or cross-linking of two or more lawsone units as previously reported through a recent theoretical and experimental effort. In that work, they determined that a lawsone dimer formed via a C-C linkage also showed a significant reduction of the $\pi \to \pi^*$ transition at 330 nm and the formation of a larger broad peak at 450 nm in DMSO.

The emission spectra of both lawsone and LPDs show similar features; however, the intensity of the excitation and emission spectrum for pure lawsone is nearly 2 orders of magnitude lower than that of the LPDs. The symmetric nature of the excitation and emission spectra and excitation independent emission suggest that the fluorescence is emanating from a molecular-like fluorophore that exists or is formed during the hydrothermal/ solvothermal process in the LPDs. This fluorophore is effectively shielded from solvent induced excited state deactivation pathways, leading to enhanced emission intensity and fluorescence quantum yield (37%), which is significantly higher than the quantum yield of pure lawsone (<0.5%). This suggests that certain electronic transitions, inherently present in lawsone, can be stabilized through some type covalent/supramolecular cross-linking or aggregation during the synthesis process. 46,47 The stabilization of these electronic states and enhanced emission are consistent with a CEE mechanism. Further analysis of the mirror symmetry shown in the excitation and emission spectra provide further evidence of a molecular-like fluorophore in the LPDs due to the observation of vibronic progression as found in other CD systems. ^{6,47,48} Vibronic progression occurs

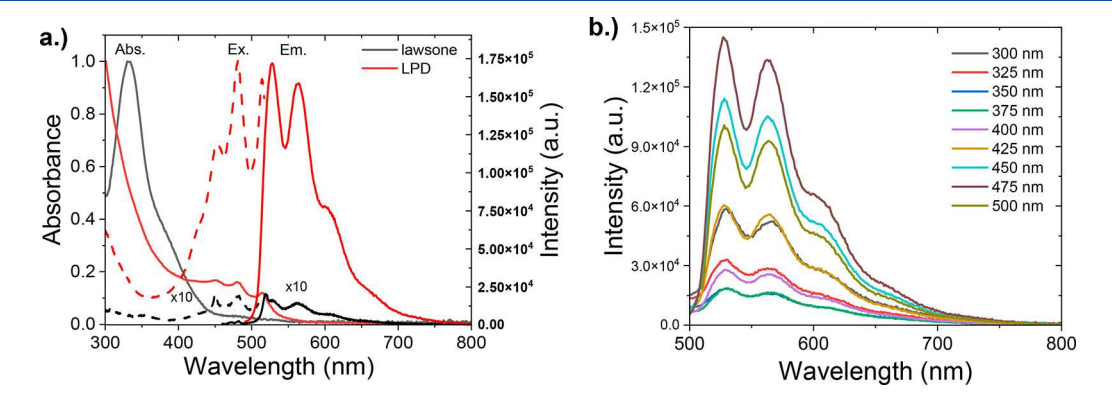


Figure 1. (a) UV-vis, excitation, and emission spectra of pure lawsone (black) and LPDs (red) in ethanol. The emission spectrum was performed with 450 nm excitation, and the excitation spectrum was performed monitoring emission at 510 nm. The excitation and emission spectra of pure lawsone was multiplied by a factor of 10 so that it can appear on scale with the LPDs. (b) Emission as a function of excitation wavelength of the LPDs. Excitation wavelengths are indicated.

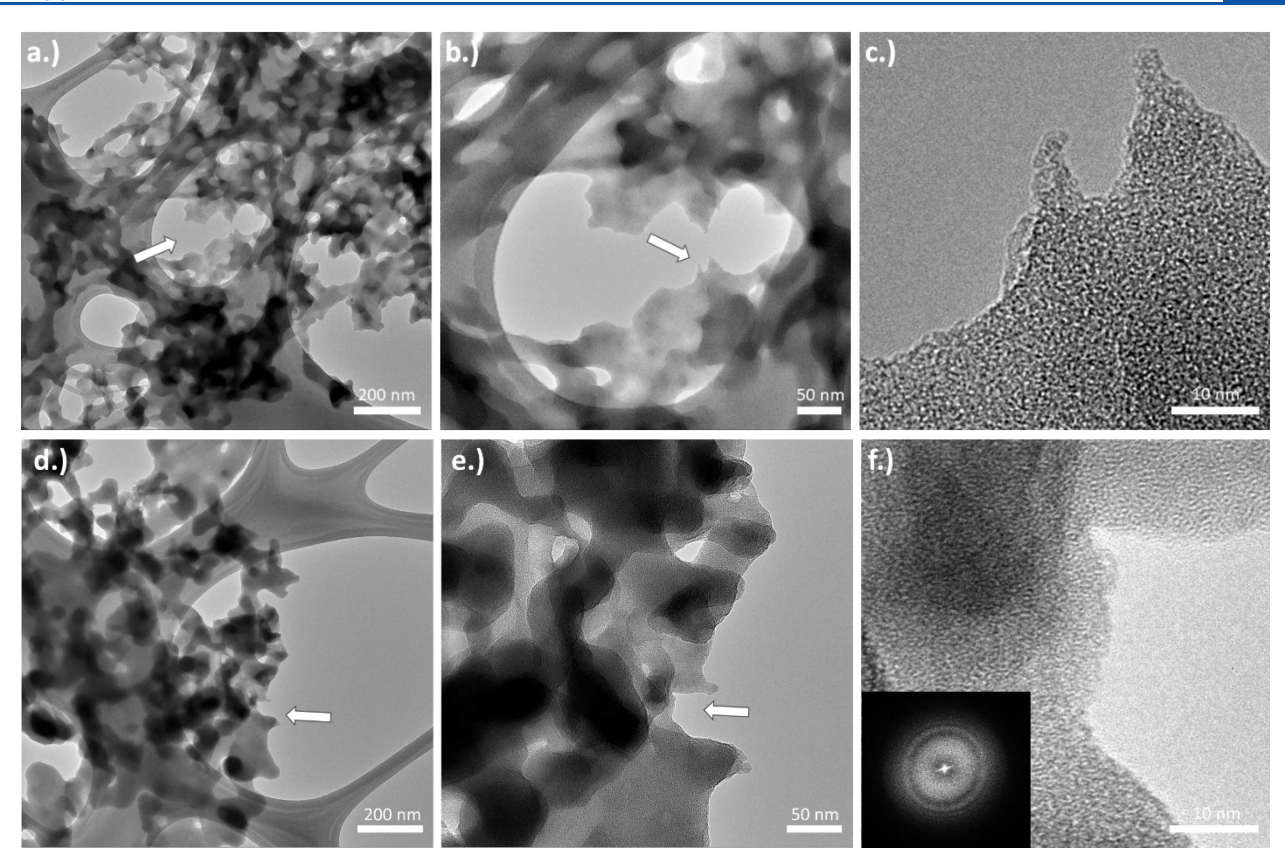


Figure 2. (a-c) TEM images of material after the first hydrothermal step at different magnifications. (d-f) TEM images of the LPD were obtained at different magnifications. The white arrows indicate the zoomed-in area of the next image. The inset in (f) is a representative of the electron diffraction pattern for these samples.

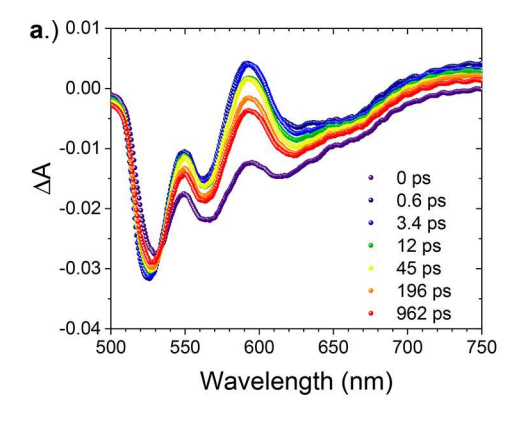
when a certain electronic transition couples with a vibrational mode to produce multiple excitation and emission peaks that are evenly spaced. The spacing in energy between the subsequent excitation and emission peaks can be correlated with the vibrational mode of a functional group. This could help to identify with which group the primary electronic transition is coupling, assuming it is only coupled to one vibrational mode. The vibronic peaks for the LPDs appear in the excitation spectrum at 429, 453, 481, and 514 nm with an average $\Delta\omega$ of 1276 cm⁻¹ between them, while the vibronic peaks in emission spectrum appear at 526, 561, 603, and 660 nm with an average $\Delta\omega$ of 1281 cm⁻¹. This calculated frequency suggests that the electronic transition could be coupling to the vibrational mode of C-O, which is proposed to occur during the cross-linking of lawsone during the hydrothermal/solvothermal process (vide infra).

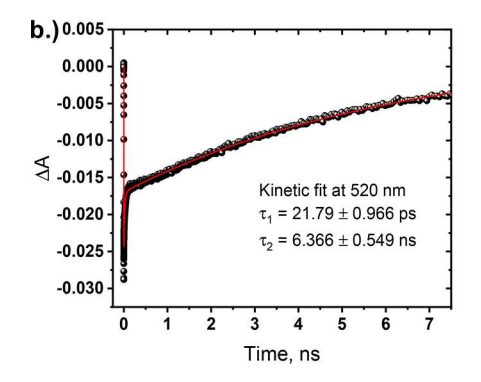
The emission map in Figure 1b shows that the LPD displays excitation independent emission. The excitation independent emission of these LPDs is in contrast to previous reports which utilized whole Henna plant (*Lawsonia inermis*) leaves, which typically contain only <2% lawsone, to prepare carbon dots. ^{41,49} They reported the commonly observed excitation dependent emission with broad peaks, which is likely due to the additional organic matter present in the Henna plant leaves.

To determine if the emission properties of the LPDs are influenced by solvent, the LPDs were desolvated via freezedrying and then redispersed in acetonitrile, THF, and DMSO (Figure S5). In these solvents, the emission spectrum still clearly shows 3 well-defined emission peaks with only a slight shift to longer wavelengths (~8 nm) for DMSO. This slight bath-

ochromic shift could be attributed the higher dipole moment and dielectric constant of DMSO (3.96 D and 47, respectively) relative to THF (1.75 D and 7.5) and acetonitrile (3.92 D and 37). The presence of DMSO could result in a small perturbation in the electronic structure on the LPD surface, which could couple with the shielded fluorophore in the core leading to a slight change in the dipole moment and the resulting emissive states. ^{50,51} Additionally, the LPDs were synthesized under different temperatures (Figure S4b-f), and soak times showed a nearly identical emission spectrum as shown in Figure 1. This could suggest that the fluorophore responsible for the observed properties is encapsulated within a polymeric structure with limited interaction with the solvent.

To obtain information about the effect of the hydrothermal (1st) and solvothermal (2nd) steps, TEM was performed on the LPD precursor after the first step (Figure 2a-c) and the LPDs (Figure 2d-f). These materials show that the nanoparticles are aggregated together in a network. Both samples are amorphous and do not show any signs of graphitization or the formation of defined crystalline domains. Their amorphous nature was also confirmed via electron diffraction, with neither sample showing crystallinity. Crystalline domains were observed only during extended imaging of the samples as a result of beam damage, which clearly showed morphological changes to the sample. The LPD precursor recovered after the first step has poorly defined nanoparticles that have a highly irregular shape with poorly defined edges. The LPDs (after the solvothermal step) show a relative reduction in particle size, along with the formation of more well-defined and rounded edges/features. The LPDs





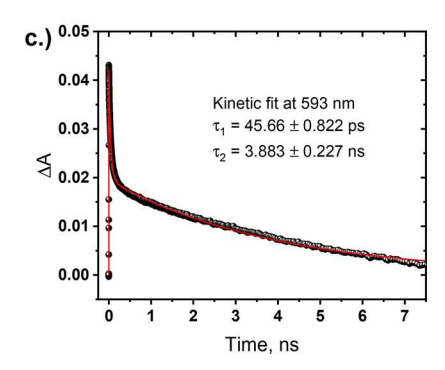


Figure 3. (a) Femtosecond transient spectra at the indicated delay times of LPDs in ethanol ($\lambda_{ex} = 480 \text{ nm}$). (b, c) TA kinetic fit of LPD decay signals at 520 and 593 nm, respectively.

resemble previously reported CPD systems, which show similar morphology and are amorphous much like carbon soot. 52–56

XPS was also performed on lawsone, the LPD precursor formed after the first step, and the LPDs (Figure S6). The C 1s spectra show a reduction in the C-O (286.2 eV) and C=O (287.7 eV) species relative to C-C and C=C (284.6 eV) going from lawsone (15.5%, 8.7%, and 75.8%, respectively) to the LPD precursor formed after the first step (4.7%, 4.3%, and 91.0%, respectively). After the second hydrothermal step and formation of the LPDs, there is a slight decrease in C-C and C=C (87.7%) and a slight increase in C=O (5.2%) and C-O stays relatively the same (4.6%). The LPDs also show the formation of a new carbon species, which is attributed to O-C=O at 288.9 eV and possible ester formation via cross-linking. The O1s XPS spectra are consistent with a reduction in the contribution of the C-O species relative to the C=O species and follow a similar trend for the same 3 samples. The TEM and XPS data suggests that the hydrothermal (1st step) facilitates the cross-linking of the lawsone units to form polymeric structures facilitated by the presence of the NaNO3 oxidant and carbonization of the polymers over 24 h to form the LPD precursor in the first step. The solvothermal step (2nd step) provides additional carbonization/cross-linking of the structure to form the smaller LPDs. This sequential polymerization and carbonization is consistent with other studies showing the impact of multiple hydro/ solvothermal steps on the photoluminescence and size of the resulting CDs.²⁶

Dynamic light scattering (DLS) was used to determine the hydrodynamic radii of LPDs synthesized as a function of temperature and time to obtain an understanding of the LPDs in the solvated state (Table S1) in comparison to the desolvated state observed in TEM. This table also summarizes the quantum

yield excited state lifetime and other spectroscopic qualities of the LPD samples. The DLS data indicates that the mean effective diameter of the LPDs shows only a slight variation and is within the range of 59 to 76 nm. This size is much larger than reported for most carbon dots, which are typically less than 10 nm, and supports the formation of larger polymer dots via extended cross-linking and carbonization. DLS showed that the LPDs possess a relatively low polydispersity in solution, which is in contrast to different sized nanoparticles shown in the TEM. This is likely due to the ultralow vacuum environment of the TEM which could cause aggregation and agglomeration of the LPDs and does not represent the true nature of the LPDs in solution.

Transient absorption (TA) spectroscopy was conducted on the starting material (lawsone) and LPDs to gain insight into their excited state dynamics. The lawsone showed one spectral feature centered at 575 nm (Figure S7a), which is ascribed to the singlet excited state. Global fit analysis yielded a one-component singlet excited lifetime of 8 ps. The decay of this excited state can be seen in Figure S7b. Due to the low fluorescence quantum yield of lawsone, we did not observe any stimulated emission in the transient spectrum. The LPDs showed more spectral characteristics with negative peaks located at 527, 623, and 620-670 nm due to stimulated emission. One positive peak, ascribed to the excited state, centered around 590 nm, and a positive band from 670 to 750 nm was deconvoluted from the spectra. Using an exponential decay fit, we found the lifetime of these positive spectral features to be around 4 ns, while the stimulated emission was found to have a lifetime of around 6 ns, which is in good agreement with fluorescence lifetime measurement. The TA spectra and kinetic fit of stimulated emission and excited state decay are shown in Figure 3.

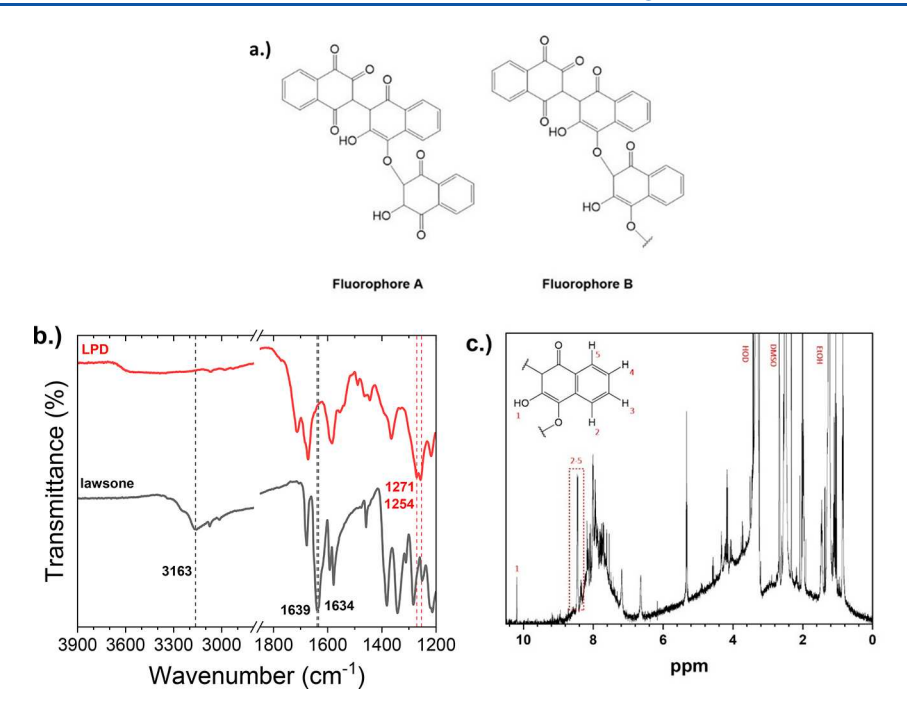


Figure 4. (a) Structure of Fluorophore A and Fluorophore B. (b) FTIR spectra of lawsone (black) and LPDs (red). (c) Proton NMR of LPDs in DMSO-d₆.

The photophysical characterization of the LPDs indicates that the fluorophore in the LPDs is likely similar to the structure of the lawone organic precursor. Assuming the fluorophore possesses a lawsone-like structure, a mechanism was proposed (Figure S8) in which cross-linking of lawsone molecules occur to form two possible candidate structures that could be present in the LPDs. The proposed mechanism is initiated by the nitrate deprotonating the hydroxyl group of lawsone (1) leading to a carbanion on structure 2, which is stabilized by the adjacent carbonyls. Then, a Michael addition reaction between the carbanion and the 4-carbon position on the α_{β} -unsaturated ketone moiety of another lawsone molecule takes place, resulting in the formation of an oxoanion on structure 3. At this point, another Michael addition reaction occurs between structure 4 and another lawsone molecule to produce 4a and 4b. If structure 4a is formed, then it may be protonated by nitric acid at the carbanion position to form structure 5 (Fluorophore A). On the condition that structure 4b is formed, it can continue polymerizing with lawsone via Michael addition producing structure 6 (Fluorophore B), which is a polymer chain. From our proposed mechanism, we suggest either Fluorophore A or Fluorophore B (Figure 4a) may be present in the structure of the LPDs. FTIR and ¹H NMR were then used to identify key structural features of the proposed fluorophore (A, B) in support of the proposed synthetic mechanism.

Figure 4b shows the FTIR spectra of lawsone (black) and the LPDs (red) in the solid state. In the spectrum of lawsone, the peaks at 3163, 1639, and 1634 cm⁻¹ correspond to C–H (α -carbon) and C=O and C=C (quinoid ring) stretching vibrations, respectively. These peaks are not present in the spectrum of the LPDs, and their disappearance is consistent with our proposed mechanism (Figure S8), suggesting that the α , β -unsaturated ketone is the reaction center of lawsone. Peaks at 1271 and 1254 cm⁻¹ are present in the spectrum of the LPDs, which may correspond to C–O stretching vibrations that result from ether linkages being formed between lawsone molecules during the synthesis.

Figure S9 shows the proton NMR spectra of pure lawsone in DMSO- d_6 and a close up of the aromatic region. The solvent peaks corresponding to DMSO and HOD (partially deuterated water) are at 2.5 and 3.3 ppm, respectively. The peaks at 11.7 and 6.2 ppm correspond to the enol proton and α -carbon proton, respectively. Analyzing the aromatic region (Figure S9b), the quartet signal at ~7.8 ppm, indicated by the red box, corresponds to the aromatic protons on lawsone.

Figure 4c shows the proton NMR spectrum of the LPDs in DMSO with a red dashed box. Surveying the spectrum below 7 ppm in the aliphatic region, numerous peaks are present that could belong to polymer chains making up the protective amorphous shell of the LPDs. We were able to identify the signal of 5 protons on the putative fluorophore in the LPDs located in the aromatic and acidic proton regions. In the ¹H NMR of the LPDs, the peak at 10.2 ppm and quartet signal at 8.2 ppm indicated by the dashed box correspond to the enol proton and benzenoid protons, respectively. These protons are significantly shifted compared to the parent lawsone molecule, which provides some insight into the new structural feature present in the LPDs. The enol proton signal is shifted upfield to 10.2 ppm (from 11.7 ppm in lawsone) and the quartet signal, shifted downfield to 8.4 ppm (from 7.8 ppm in lawsone). The upfield shift of the enol proton is a result of increased shielding. Increased shielding could be caused by formation of the ether bond on the adjacent carbonyl, eliminating a strong electron withdrawing group. The downfield shift of the quartet signal is a result of electron density being withdrawn from the benzenoid ring, resulting in the deshielding of these protons. Increased deshielding could be caused by the π -bond shifting position next to the benzenoid ring. Extending conjugation throughout the putative fluorophore causes the benzenoid ring to lose aromaticity, allowing the adjacent carbonyl to withdraw its electron density. The peak at 15.1 ppm is indicative of a strong hydrogen bond taking place between a hydroxyl group and a carbonyl which may be present between two adjacent units of cross-linked lawsone chains of fluorophore B as depicted in

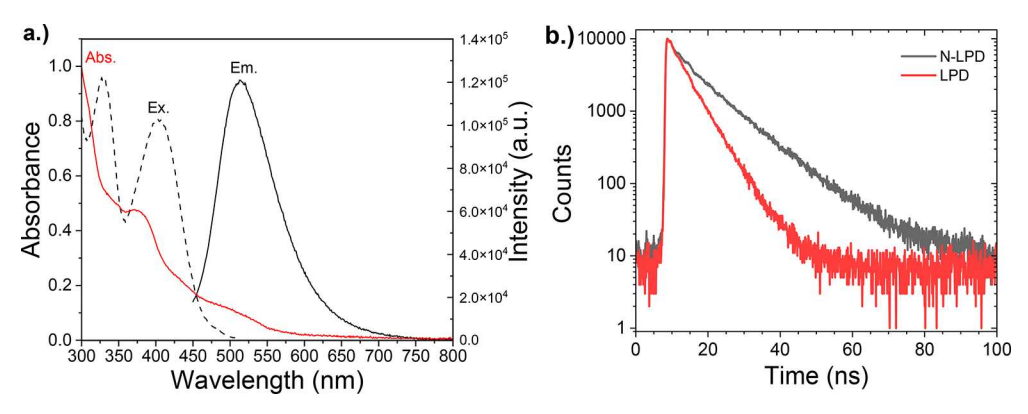


Figure 5. (a) UV—vis (solid red line), excitation (dashed black line), and emission (solid black line) spectra of the N-LPDs. (b) Fluorescent lifetime measurement of the N-LPDs compared to the LPDs.

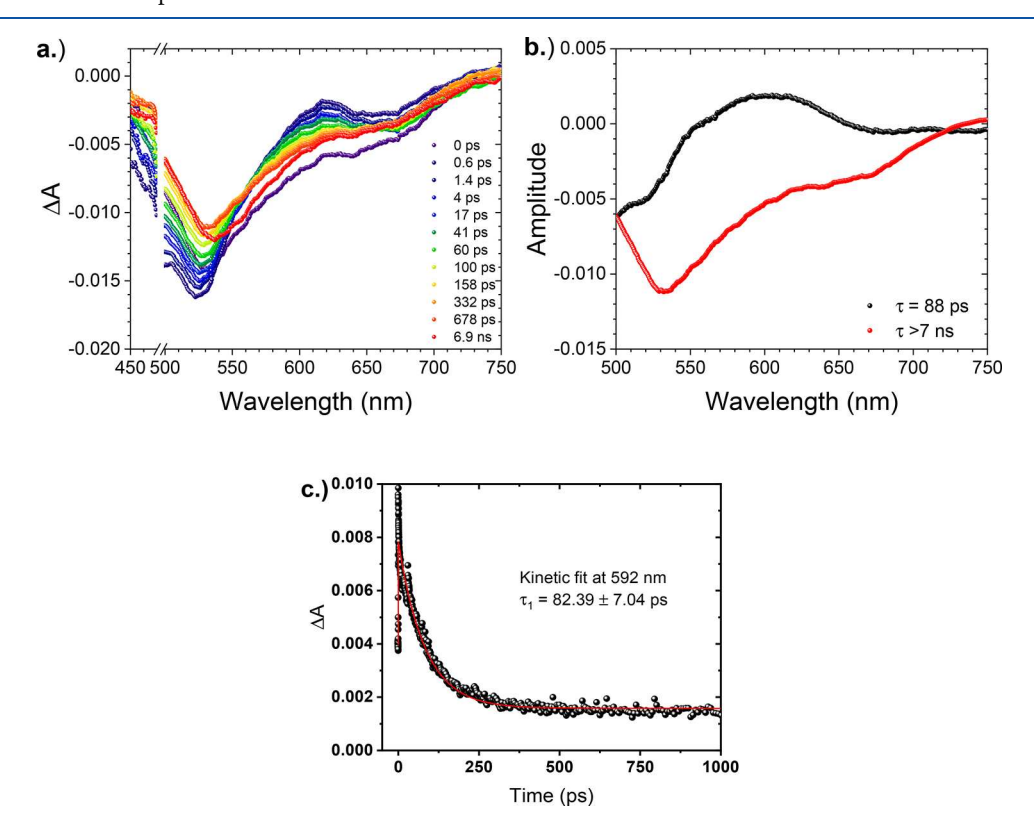


Figure 6. (a) Femtosecond transient spectra at the indicated delay times of N-LPDs in ethanol (λ_{ex} = 480 nm). (b) Decay associated spectra of N-LPD TA data. Black line indicates excited state, and red line indicates stimulated emission. (c) TA kinetic fit of N-LPD excited state decay at 592 nm.

Figure S10. We note that there could be other potential pathways to form other dimers, trimers, or higher-order cross-linked polymer structures during the hydrothermal/solvothermal process. Additionally, these structures may also cross-link among themselves to form additional 3-D structures within the LPDs.

3.3. TD-DFT Calculations. Based on the proposed cross-linking mechanism and the chemical features of the LPDs proposed by FTIR and NMR, both fluorophores A and B were modeled using density functional theory (DFT) and time dependent—density functional theory (TD-DFT). Figure S11a shows the solid state theoretical FTIR of fluorophore A (red) and fluorophore B (blue) compared to the experimental (black) spectra of the LPDs. Surveying the simulated spectra of fluorophore A, the peak at $\sim 1300~\rm cm^{-1}$, with a strong intensity, corresponds to C–O stretching vibrations of an ether bond in the structure. The C–O stretching peak in the spectra of

fluorophore A is slightly shifted to a higher wavenumber compared to the experimental spectra. When the spectra of fluorophore B were compared to the experimental spectra, there were no similar peaks between them. The theoretical UV-vis spectra (Figure S11b) of fluorophore A (red) and fluorophore B (blue) were compared to the experimental spectra (black), which show similar absorption profiles to the LPDs. Fluorophore A has an absorption peak occurring at 471 nm, and fluorophore B has peaks at 454 and 511 nm. These peaks are near the ones that are present in the LPD spectra at 450, 481, and 515 nm. Figure S11c shows the molecular orbitals of the HOMO and LUMO energy levels for each electron transition occurring from fluorophores A and B. The overlap of the theoretical UV-vis of fluorophores A and B with the LPD UVvis suggests that these fluorophores or similar structural motifs could be present in the LPDs.

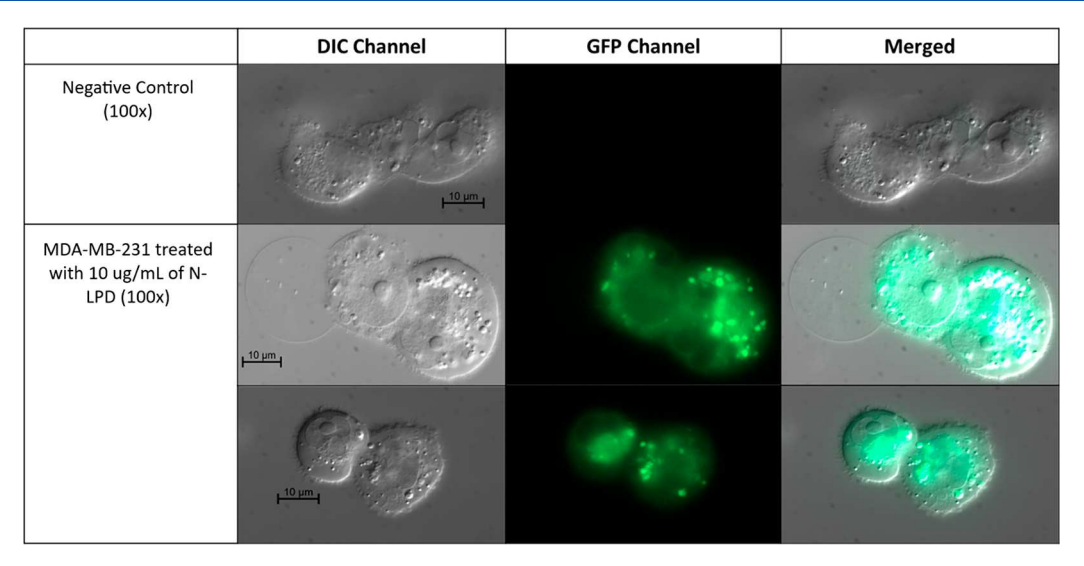


Figure 7. Microscopy images of individual MDA-MB-231 cells treated and not treated (negative control) with 10 μ g/mL N-LPDs at 100× magnification.

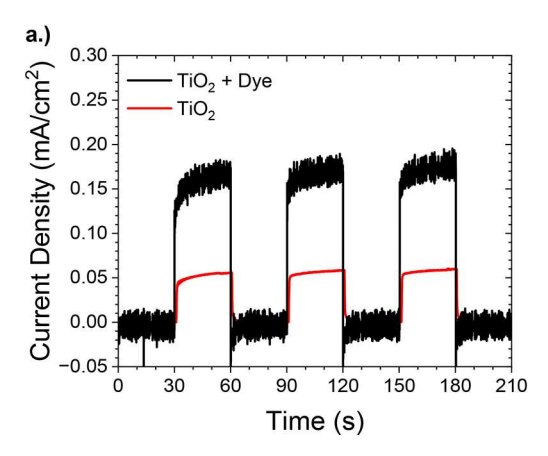
3.4. Synthesis and Characterization of Nitrogen Doped-Lawsone Polymer Dots (N-LPDs). Although the LPDs provided unique photophysical properties and an opportunity to possibly identify the fluorophore(s) responsible for emission, they are relatively insoluble and their fluorescence is quenched in water. This would significantly limit their utility in many applications, such as fluorescence microscopy dyes for biological systems. To overcome this drawback, hydrophilic amine (-NH₂) functional groups were introduced through the addition of diethylene triamine during the synthesis. The resulting N-LPDs had a fluorescence quantum yield of 24% with good solubility in water compared to the base LPDs. Figure 5a shows the absorption, excitation, and emission spectra of the N-LPDs. The absorption spectra show that the N-LPDs have a broad absorption range with a peak at 375 nm. On the excitation spectra, peaks appear at 330 and 405 nm, and the emission spectra shows a single peak at 515 nm.

The fluorescence lifetime measurement of the N-LPDs (Figure 5b) also shows a single exponential decay but with a lifetime of 9.9 ns which is significantly higher than the 5.1 ns of the base LPDs. Since the fluorescence lifetime is an intrinsic property related to the molecular structure of the fluorophore, it is likely the fluorophore of the N-LPDs has a different structure from the base LPDs. This is also apparent in the excitation and emission spectrum of the N-LPDs which does not display the vibronic progression as observed for the single component LPD. The FTIR of the N-LPDs shows clear shifts in the N-H and C-N vibrational modes relative to the diethylenediamine which is consistent with its attachment and incorporation in the N-LPDs (Figure S12a). XPS of the N-LPDs clearly shows the incorporation of nitrogen into the N-LPD structure (Figure S13) and the appearance of C-N-C and N-H species at 399.0 and 401.8 eV, respectively. The UV-vis, excitation, and emission map spectra are also different when compared with the LPDs (Figure S12b). TEM images of the N-LPDs show a slightly smaller particle size than the LPDs without the introduction of diethylenediamine (Figure S12c). The functionalization of lawsone with primary and secondary amines is known to occur in solvents like ethanol. 57,58 This is likely due to the attachment of the diethylene triamine via the terminal primary or central secondary amine to the 4-carbon position on

the α , β -unsaturated ketone of lawsone, which could hinder the subsequent addition of another lawsone unit as described in the proposed mechanism in the Supporting Information for LPD formation (Figure S8) or could lead to other cross-linking pathways. The additional reaction pathways/products due to the incorporation of diethylene triamine into the N-LPD structure likely results in new, but similar, emissive states in the material. S9 As a result, the new emissive states could couple with each other, leading to a broad and featureless emission profile as observed. However, it is important to point out that the N-LPDs also exhibit excitation independent emission, which suggests that the emissive core is likely stabilized through the cross-linked enhanced emission effect. The CIE 1931 analysis (Figure S12d) shows the emission color of the N-LPDs lies further into the green region of the chromatic diagram compared to the LPDs.

Transient absorption analysis of the N-LPDs (Figure 6a) showed a wide negative signal across the measurement range mirroring that of the steady-state emission shown in Figure 5a. After subjecting the data to global fit analysis, one positive feature that spanned the measurement range with a peak maximum at 592 nm was deconvoluted which is ascribed to an excited state. This excited state had a short-lived lifetime of approximately 88 ps. We were unable to extrapolate the stimulated emission lifetime from the TA data due to the complete overlap of the excited state decay signal on the stimulated emission recovery signal. The decay associated spectra and fit decay of the excited state are reported in Figure 6b,c, respectively.

3.5. Cytotoxicity and Fluorescence Microscopy. Owing to the enhanced water solubility of the N-LPDs, they were selected as candidates for use as fluorescence microscopy dyes for imaging triple negative breast cancer cells MDA-MB-231. Cytotoxicity analysis utilizing a MTT (3-(4,5-dimethylthiazol-2-yl)-2,5-diphenyltetrazolium) assay was performed to determine the compatibility of the N-LPDs with the MDA-MB-231 cells and determine the usable N-LPD concentration range for fluorescence imaging studies (Figure S14). Based on the MTT assays, it was determined that a concentration of less than $10 \, \mu g/m$ ML N-LPDs would be optimal, since the MDA-MB-231 cell viability was unaffected at these levels.



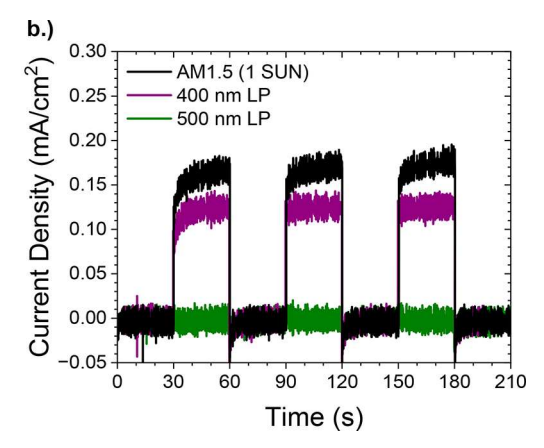


Figure 8. Photocurrent density vs time plots of TiO₂ and TiO₂-LPD devices under AM1.5 (1 sun) illumination (A) and under various filtered conditions (B).

Fluorescence microscopy was performed to confirm that the N-LPDs were taken up by the MDA-MB-231 cells. The cells were incubated with the N-LPDs for 24 h at a concentration of $10~\mu g/mL$. Prior to imaging, the cells were rinsed three times with phosphate buffer saline to remove any residual media and N-LPDs bound to the surface of the cells. Figure S15 shows wide-field images of multiple cells treated with and without the N-LPDs at a magnification of $10\times$. The DIC channel for both samples shows outlines of the cells appearing as light specks on the grayish background. The GFP channel exhibits a green fluorescent signal in cells treated with N-LPDs but no signal in negative controls. Merged images show the GFP fluorescent signal localizing with the cells in the wide-field images.

To achieve a more detailed view, images of individual cells at a magnification of 100× (Figure 7) were also collected. Examples of the cells at this magnification are shown in the DIC channel for both the negative control and cells treated with N-LPDs. The GFP signal observed in the N-LPD-treated cells suggests that the fluorescence originated from inside the cells. The merged image further shows that the GFP signal appears colocalized with structures visible in the cells. To prove whether the GFP signal was emanating from inside the cells, Z-stacks were acquired on individual cells (Figure S16 and Video S1). These data show the strongest signal colocalized to the center Z-slices of the cell, confirming the uptake of the N-LPDs into the cell. Analyzing the GFP images, the signal appears to be distributed throughout the entire cell, but there are puncta of different sizes scattered throughout the cell in which the signal intensity appears to be the highest. The signal of these puncta may overlap the vacuoles in the cell, indicating their accumulation within these organelles, but further investigation would be required to establish with certainty which structures they are. Since vacuoles help sequester waste products and the signal may be localized in this organelle, it suggests that the N-LPDs currently lack the ability to localize within specific regions of the cell which is common for many CD based fluorescent microscopy dyes. However, with the presence of the amine groups in the N-LPDs, it may be possible to chemically functionalize and attach site selective groups to the N-LPDs that favor accumulations in specific regions within the cell to increase their utility as dyes.

3.6. DSSC Fabrication and Testing. Owing to the photophysical properties and sustainable nature of the plant based lawsone molecule, it has received interest as a photosensitizer dye in a DSSC from theoretical and experimental approaches. 43–45,60–62 The utility of lawone for this application

has been realized through its incorporation into composites. For example, composites containing lawsone have been demonstrated via incorporation into transition metal complexes (with Fe²⁺, Cr³⁺, Co²⁺, Zn²⁺) as a ligand, 63 attached to silver nanoparticles, 43 derivatized with thiophenyls, 64 or paired with betanin as a cosensitizer. 65 These composites have been shown to be compatible with both TiO2 and ZnO photoanode based materials. 44,65,66 The power conversion efficiencies for these devices range from 0.2% to 2.85%. As a proof-of-concept demonstration that LPDs could be used as a photosensitizer for organic photovoltaics, a DSSC was fabricated and evaluated. The components, energetics, and critical dynamic events are depicted in Figure S17. The DSSCs were composed of TiO₂ or TiO2-LPDs as photoanodes, a platinum cathode, and an electrolyte containing 0.1 M 1-butyl-3-methylimidazolium iodide (BMII), 0.01 M I₂, and 0.1 M 4-tert-butylpyridine (TBP) in an ethylene glycol solution. The TiO₂-LPD anode was prepared by first doctor blading and sintering a TiO2 paste (produced from stirring TiO₂ nanopowder with polyethylene glycol (PEG) overnight) on fluorine doped tin oxide (FTO) coated glass and then soaking TiO₂ in a concentrated solution of LPDs in EtOH. The extent of the loading was monitored via UV—vis, and upon soaking, a new low-energy absorption feature from 400 to 600 nm can be observed for TiO2-LPD film that is not present for the TiO2 only film. This absorption feature is consistent with the absorption onset of LPDs in solution (Figures S18 and S19). Iodide was chosen as the redox mediator because its redox couple (0.35 V vs SHE) is sufficiently capable of regenerating the ground state of the LPDs and is a commonly used and well-behaved redox mediator for DSSCs.⁶⁷

The excited state potential for the LPDs was calculated using $E_{1/2}{}^*=E_{1/2}{}^{\rm OX}-\Delta G_{\rm ES}$, where $E_{1/2}{}^{\rm OX}$ is the ground state oxidation potential of the LPDs (0.79 V vs SHE) as determined though cyclic voltammetry (Figure S20) and $\Delta G_{\rm ES}$ is the thermally equilibrated lowest-energy excited state which we obtained by calculating the direct allowed transition from the valence band to the conduction band of the LPDs (5.88 eV, 1.38 V vs normal hydrogen electrode, NHE) via Tauc plot analysis (Figure S21). The excited state potential of LPDs ($E_{1/2}{}^*=-0.59~{\rm V}~{\rm vs}~{\rm NHE}$), while low (<100 mV greater than that of the conduction band of TiO₂), is still sufficient for excited state electron transfer ($k_{\rm inj}$) to occur from the excited state of the LPDs to the conduction band of TiO₂ ($E_{\rm CB}=-0.5~{\rm V}~{\rm vs}~{\rm NHE}$). Additionally, following electron injection, there is a >400 mV

driving force for regeneration of the oxidized dye by iodide/triiodide (0.35 V vs NHE).

Photocurrent density-voltage (J-V) curves for the devices containing either TiO2 or TiO2-LPD photoanodes were acquired, and the results are shown in Figure S22 with the relevant metrics reported in Table S2. To demonstrate the feasibility of using LPDs as a sensitizer in DSSC applications, current density—time (J-T) plots were obtained in which the devices were illuminated with solar simulated light at AM1.5 (1 sun) intensity in 30 s intervals (Figure 8). It was observed that the TiO₂-LPD device had a 3-fold improvement in photocurrent density which agrees with the observed increase in J_{SC} previously seen in the J-V analysis. When wavelengths in the maximum absorbance window for TiO₂ (<400 nm) were filtered out, we observed a decrease in photocurrent density of ~ 0.05 mA cm⁻², which is comparable to the amount of photocurrent generated by the TiO₂ only device. Assuming the LPDs were the primary component contributing to photocurrent generation under that filtered condition, then it is fair to assume that 0.12 of the 0.17 mA cm² generated when fully illuminated could be attributed to the LPDs (70%). Additionally, when wavelengths in the maximum absorbance window for both TiO2 and LPDs were filtered out (<500 nm), it was found that the device produced negligible or no discernible photocurrent upon illumination, suggesting that the TiO2 and LPD maximum absorbance windows are the main areas for light absorption and photocurrent generation in this device.

4. CONCLUSIONS

In this study, we developed and demonstrated a two-step pathway to producing lawson polymer dots (LPDs) with the ability to remove small molecule organic fluor impurities commonly produced in similar systems and evaluate the possible CEE effect. The high quantum yield (37%) and molecular-like fluorescence of the LPDs are attributed to the formation of a lawsone based cross-linked structure which is effectively shielded from solvent induced, nonradiative quenching pathways, while enhancing the inherent emissive properties of the molecular fluorophore. A series of spectroscopic studies provide a pathway to understanding the possible mechanism of the LPD formation and candidate fluorophores that could be responsible for the observed behavior. This approach can be readily adapted to other similar single component carbon dot systems, leading to a deeper understanding of the formation mechanism and possible methodology to fine-tune their emissive properties. We also developed a water-soluble lawsone polymer dot (N-LPD) and demonstrated its feasibility as a fluorescence microscopy dye to image breast cancer cells, and proof-of-concept DSSCs validated the feasibility of using the LPDs as a sensitizer for solar harvesting applications.

ASSOCIATED CONTENT

Supporting Information

The Supporting Information is available free of charge at https://pubs.acs.org/doi/10.1021/acsanm.3c03229.

Video S1 showing Z-stack images (AVI) Additional characterization of the LPDs (PDF)

AUTHOR INFORMATION

Corresponding Authors

Joseph A. Teprovich, Jr. – Department of Chemistry & Biochemistry, California State University Northridge,

Northridge, California 91330, United States; orcid.org/0000-0002-7285-4844; Email: joseph.teprovich@csun.edu

Patrick A. Ward — Materials Technology and Energy Division, Savannah River National Laboratory, Aiken, South Carolina 29803, United States; oorcid.org/0000-0003-1179-9228; Email: patrick.ward@srnl.doe.gov

Authors

Jesus Hernandez — Department of Chemistry & Biochemistry, California State University Northridge, Northridge, California 91330, United States; Oorcid.org/0000-0002-7322-5054

Alex Robb — Materials Technology and Energy Division, Savannah River National Laboratory, Aiken, South Carolina 29803, United States

Savannah Servera – Department of Chemistry & Biochemistry, California State University Northridge, Northridge, California 91330, United States

Nanor Bedrosian – Department of Chemistry & Biochemistry, California State University Northridge, Northridge, California 91330, United States

Osma Gomez – Department of Chemistry & Biochemistry, California State University Northridge, Northridge, California 91330, United States

Zachary Duca — Materials Technology and Energy Division, Savannah River National Laboratory, Aiken, South Carolina 29803, United States

Michael B. Thomas – Materials Technology and Energy Division, Savannah River National Laboratory, Aiken, South Carolina 29803, United States

Daniel Tamae – Department of Chemistry & Biochemistry, California State University Northridge, Northridge, California 91330, United States

Paula L. Fischhaber – Department of Chemistry & Biochemistry, California State University Northridge, Northridge, California 91330, United States

Simon J. Garrett — Department of Chemistry & Biochemistry, California State University Northridge, Northridge, California 91330, United States; orcid.org/0000-0002-7710-8488

Complete contact information is available at: https://pubs.acs.org/10.1021/acsanm.3c03229

Notes

The authors declare no competing financial interest.

ACKNOWLEDGMENTS

This work was supported by the Laboratory Directed Research and Development (LDRD) program within the Savannah River National Laboratory (SRNL). This work was produced by Battelle Savannah River Alliance, LLC under Contract No. 89303321CEM000080 with the U.S. Department of Energy. Publisher acknowledges the U.S. Government license to provide public access under the DOE Public Access Plan (https://www. energy.gov/downloads/doe-public-access-plan). The theoretical work and TD-DFT calculations performed at California State University Northridge (CSUN) was supported by the NSF MRI grant program (award # 2117956). J.H. would like to acknowledge the NIH-T32GM137863 training grant for support to conduct this research. D.T. would like to acknowledge the National Institute of Health grant SC2GM130471 for the work with the MDA-MB-231 cell line. P.L.F. would like to acknowledge the National Institute of Health grant SC1GM127204 for the fluorescence microscopy studies.

REFERENCES

- (1) Xu, X.; Ray, R.; Gu, Y.; Ploehn, H. J.; Gearheart, L.; Raker, K.; Scrivens, W. A. Electrophoretic Analysis and Purification of Fluorescent Single-Walled Carbon Nanotube Fragments. *J. Am. Chem. Soc.* **2004**, 126, 12736–12737.
- (2) Fei, H.; Ye, R.; Ye, G.; Gong, Y.; Peng, Z.; Fan, X.; Samuel, E. L. G.; Ajayan, P. M.; Tour, J. M. Boron- and Nitrogen-Doped Graphene Quantum Dots/Graphene Hybrid Nanoplatelets as Efficient Electrocatalysts for Oxygen Reduction. ACS Nano 2014, 8, 10837–10843.
- (3) Su, W.; Guo, R.; Yuan, F.; Li, Y.; Li, X.; Zhang, Y.; Zhou, S.; Fan, L. Red-Emissive Carbon Quantum Dots for Nuclear Drug Delivery in Cancer Stem Cells. J. Phys. Chem. Lett. 2020, 11, 1357–1363.
- (4) Suzuki, N.; Wang, Y.; Elvati, P.; Qu, Z.-B.; Kim, K.; Jiang, S.; Baumeister, E.; Lee, J.; Yeom, B.; Bahng, J. H.; et al. Chiral Graphene Quantum Dots. ACS Nano 2016, 10, 1744–1755.
- (5) Sun, Y.-P.; Zhou, B.; Lin, Y.; Wang, W.; Fernando, K. A. S.; Pathak, P.; Meziani, M. J.; Harruff, B. A.; Wang, X.; Wang, H.; et al. Quantum-Sized Carbon Dots for Bright and Colorful Photoluminescence. *J. Am. Chem. Soc.* **2006**, *128*, 7756–7757.
- (6) Soni, N.; Singh, S.; Sharma, S.; Batra, G.; Kaushik, K.; Rao, C.; Verma, N. C.; Mondal, B.; Yadav, A.; Nandi, C. K. Absorption and emission of light in red emissive carbon nanodots. *Chem. Sci.* **2021**, *12*, 3615–3626.
- (7) Zhang, T.; Zhao, F.; Li, L.; Qi, B.; Zhu, D.; Lü, J.; Lü, C. Tricolor White-Light-Emitting Carbon Dots with Multiple-Cores@Shell Structure for WLED Application. ACS Appl. Mater. Interfaces 2018, 10, 19796—19805.
- (8) Wang, L.; Zhu, S.-J.; Wang, H.-Y.; Qu, S.-N.; Zhang, Y.-L.; Zhang, J.-H.; Chen, Q.-D.; Xu, H.-L.; Han, W.; Yang, B.; et al. Common Origin of Green Luminescence in Carbon Nanodots and Graphene Quantum Dots. ACS Nano 2014, 8, 2541–2547.
- (9) Liu, J.; Li, D.; Zhang, K.; Yang, M.; Sun, H.; Yang, B. One-Step Hydrothermal Synthesis of Nitrogen-Doped Conjugated Carbonized Polymer Dots with 31% Efficient Red Emission for In Vivo Imaging. *Small* **2018**, *14*, No. 1703919.
- (10) Shao, J.; Zhu, S.; Liu, H.; Song, Y.; Tao, S.; Yang, B. Full-Color Emission Polymer Carbon Dots with Quench-Resistant Solid-State Fluorescence. *Ad. Sci.* **2017**, *4*, No. 1700395.
- (11) Das, P.; Bhattacharyya, S. K.; Banerji, P.; Das, N. C. Acoustic cavitation assisted synthesis and characterization of photoluminescent carbon quantum dots for biological applications and their future prospective. *Nano-Struct. Nano-Objects* **2021**, 25, 100641.
- (12) Bhattacharyya, S. K.; Jana, I. D.; Pandey, N.; Biswas, D.; Girigoswami, A.; Dey, T.; Banerjee, S.; Ray, S. K.; Mondal, A.; Mukherjee, G.; et al. Ho3+-Doped Carbon Dot/Gelatin Nanoparticles for pH-Responsive Anticancer Drug Delivery and Intracellular Cu2+ Ion Sensing. ACS Appl. Nano Mater. 2022, 5 (8), 11809–11822.
- (13) Rasal, A. S.; Yadav, S.; Yadav, A.; Kashale, A. A.; Manjunatha, S. T.; Altaee, A.; Chang, J.-Y. Carbon Quantum Dots for Energy Applications: A Review. ACS Appl. Nano Mater. 2021, 4, 6515–6541.
- (14) Hinterberger, V.; Damm, C.; Haines, P.; Guldi, D. M.; Peukert, W. Purification and structural elucidation of carbon dots by column chromatography. *Nanoscale* **2019**, *11*, 8464–8474.
- (15) Reckmeier, C. J.; Schneider, J.; Xiong, Y.; Häusler, J.; Kasák, P.; Schnick, W.; Rogach, A. L. Aggregated Molecular Fluorophores in the Ammonothermal Synthesis of Carbon Dots. *Chem. Mater.* **2017**, 29, 10352–10361.
- (16) Mruthunjayappa, M. H.; Kotrappanavar, N. S.; Mondal, D. New prospects on solvothermal carbonisation assisted by organic solvents, ionic liquids and eutectic mixtures A critical review. *Prog. Mater. Sci.* **2022**, *126*, No. 100932.
- (17) Cayuela, A.; Soriano, M. L.; Carrillo-Carrión, C.; Valcárcel, M. Semiconductor and carbon-based fluorescent nanodots: the need for consistency. *Chem. Commun.* **2016**, *52*, 1311–1326.
- (18) Campbell, E.; Hasan, M. T.; Gonzalez Rodriguez, R.; Akkaraju, G. R.; Naumov, A. V. Doped Graphene Quantum Dots for Intracellular Multicolor Imaging and Cancer Detection. *ACS Biomater. Sci. Eng.* **2019**, *5*, 4671–4682.

- (19) Cho, H.-H.; Yang, H.; Kang, D. J.; Kim, B. J. Surface Engineering of Graphene Quantum Dots and Their Applications as Efficient Surfactants. ACS Appl. Mater. Interfaces 2015, 7, 8615–8621.
- (20) Ye, R.; Peng, Z.; Metzger, A.; Lin, J.; Mann, J. A.; Huang, K.; Xiang, C.; Fan, X.; Samuel, E. L. G.; Alemany, L. B.; et al. Bandgap Engineering of Coal-Derived Graphene Quantum Dots. *ACS Appl. Mater. Interfaces* **2015**, *7*, 7041–7048.
- (21) Dong, Y.; Wang, R.; Li, G.; Chen, C.; Chi, Y.; Chen, G. Polyamine-Functionalized Carbon Quantum Dots as Fluorescent Probes for Selective and Sensitive Detection of Copper Ions. *Anal. Chem.* **2012**, *84*, 6220–6224.
- (22) Tong, L.; Wang, X.; Chen, Z.; Liang, Y.; Yang, Y.; Gao, W.; Liu, Z.; Tang, B. One-Step Fabrication of Functional Carbon Dots with 90% Fluorescence Quantum Yield for Long-Term Lysosome Imaging. *Anal. Chem.* **2020**, 92, 6430–6436.
- (23) Tao, S.; Feng, T.; Zheng, C.; Zhu, S.; Yang, B. Carbonized Polymer Dots: A Brand New Perspective to Recognize Luminescent Carbon-Based Nanomaterials. *J. Phys. Chem. Lett.* **2019**, *10*, 5182–5188.
- (24) Cong, S.; Jiang, Z.; Zhang, R.; Lv, H.; Guo, J.; Zhang, L.; Lu, X. Polymer Carbon Nanodots: A Novel Electrochemiluminophore for Dual Mode Detection of Ferric Ions. *Anal. Chem.* **2022**, *94*, 6695–6702
- (25) Zhu, S.; Song, Y.; Zhao, X.; Shao, J.; Zhang, J.; Yang, B. The photoluminescence mechanism in carbon dots (graphene quantum dots, carbon nanodots, and polymer dots): current state and future perspective. *Nano Res.* **2015**, *8*, 355–381.
- (26) Liu, J.; Li, R.; Yang, B. Carbon Dots: A New Type of Carbon-Based Nanomaterial with Wide Applications. *ACS Cent. Sci.* **2020**, *6*, 2179–2195.
- (27) Zhu, S.; Song, Y.; Shao, J.; Zhao, X.; Yang, B. Non-Conjugated Polymer Dots with Crosslink-Enhanced Emission in the Absence of Fluorophore Units. *Angew. Chem., Int. Ed.* **2015**, *54*, 14626–14637.
- (28) Tao, S.; Zhu, S.; Feng, T.; Zheng, C.; Yang, B. Crosslink-Enhanced Emission Effect on Luminescence in Polymers: Advances and Perspectives. *Angew. Chem., Int. Ed.* **2020**, *59*, 9826–9840.
- (29) Kim, J. Y.; Kim, B. G.; Kim, M.; Jang, W.; Wang, D. H. One-step formation of core/shell structure based on hydrophobic silane ligands for enhanced luminescent perovskite quantum dots. *J. Alloys Compd.* **2021**, *886*, No. 161347.
- (30) Zeng, Y.; Chen, W.; Deng, Y.; Gu, W.; Wu, C.; Guo, Y.; Huang, P.; Liu, F.; Li, H. FAPbBr3/Cs4PbBr6 Core/Shell Perovskite Nanocrystals with Enhanced Stability and Emission: Implications for LEDs. ACS Appl. Mater. Interfaces 2022, 5, 9534–9543.
- (31) Mishra, K.; Barai, M.; Ghosh, S. Roles of Impurity and Sample Heterogeneity in Intriguing Photoluminescence Properties of Zero-Dimensional (0D) Carbonaceous Materials. *J. Phys. Chem. C* **2022**, *126*, 16905–16918.
- (32) Xiong, Y.; Schneider, J.; Ushakova, E. V.; Rogach, A. L. Influence of molecular fluorophores on the research field of chemically synthesized carbon dots. *Nano Today* **2018**, 23, 124–139.
- (33) Essner, J. B.; Kist, J. A.; Polo-Parada, L.; Baker, G. A. Artifacts and Errors Associated with the Ubiquitous Presence of Fluorescent Impurities in Carbon Nanodots. *Chem. Mater.* **2018**, *30*, 1878–1887.
- (34) de Boëver, R.; Town, J. R.; Li, X.; Claverie, J. P. Carbon Dots for Carbon Dummies: The Quantum and The Molecular Questions Among Some Others. *Chem.—Eur. J.* **2022**, 28, No. e202200748.
- (35) Song, Y.; Zhu, S.; Zhang, S.; Fu, Y.; Wang, L.; Zhao, X.; Yang, B. Investigation from chemical structure to photoluminescent mechanism: a type of carbon dots from the pyrolysis of citric acid and an amine. *J. Mater. Chem. C* **2015**, *3*, 5976–5984.
- (36) Zhang, J.; Yang, L.; Yuan, Y.; Jiang, J.; Yu, S.-H. One-Pot Gram-Scale Synthesis of Nitrogen and Sulfur Embedded Organic Dots with Distinctive Fluorescence Behaviors in Free and Aggregated States. *Chem. Mater.* **2016**, 28, 4367–4374.
- (37) Das, A.; Gude, V.; Roy, D.; Chatterjee, T.; De, C. K.; Mandal, P. K. On the Molecular Origin of Photoluminescence of Nonblinking Carbon Dot. *J. Phys. Chem. C* **2017**, *121*, 9634–9641.

- (38) Hu, Q.; Meng, X.; Chan, W. An investigation on the chemical structure of nitrogen and sulfur codoped carbon nanoparticles by ultraperformance liquid chromatography-tandem mass spectrometry. *Anal. Bioanal. Chem.* **2016**, *408*, 5347–5357.
- (39) Fuyuno, N.; Kozawa, D.; Miyauchi, Y.; Mouri, S.; Kitaura, R.; Shinohara, H.; Yasuda, T.; Komatsu, N.; Matsuda, K. Drastic Change in Photoluminescence Properties of Graphene Quantum Dots by Chromatographic Separation. *Adv. Opt. Mater.* **2014**, *2*, 983–989.
- (40) Vinci, J. C.; Ferrer, I. M.; Seedhouse, S. J.; Bourdon, A. K.; Reynard, J. M.; Foster, B. A.; Bright, F. V.; Colón, L. A. Hidden Properties of Carbon Dots Revealed After HPLC Fractionation. *J. Phys. Chem. Lett.* **2013**, *4*, 239–243.
- (41) Shahshahanipour, M.; Rezaei, B.; Ensafi, A. A.; Etemadifar, Z. An ancient plant for the synthesis of a novel carbon dot and its applications as an antibacterial agent and probe for sensing of an anti-cancer drug. *Mater. Sci. Eng.*, C **2019**, *98*, 826–833.
- (42) Wang, Z.; Yuan, F.; Li, X.; Li, Y.; Zhong, H.; Fan, L.; Yang, S. 53% Efficient Red Emissive Carbon Quantum Dots for High Color Rendering and Stable Warm White-Light-Emitting Diodes. *Adv. Mater.* **2017**, 29, No. 1702910.
- (43) Sreeja, S.; Pesala, B. Plasmonic enhancement of betanin-lawsone co-sensitized solar cells via tailored bimodal size distribution of silver nanoparticles. *Sci. Rep.* **2020**, *10*, 8240.
- (44) Khadtare, S. S.; Ware, A. P.; Salunke-Gawali, S.; Jadkar, S. R.; Pingale, S. S.; Pathan, H. M. Dye sensitized solar cell with lawsone dye using a ZnO photoanode: experimental and TD-DFT study. *RSC Adv.* **2015**, *5*, 17647–17652.
- (45) Makoye, A.; Pogrebnoi, A.; Pogrebnaya, T. Lawsone isomers, lawsone ether and bilawsone for dye-sensitized solar cells applications: DFT and UV-Vis studies. *J. Mol. Graph Model.* **2020**, *94*, No. 107457.
- (46) Zhu, S.; Wang, L.; Zhou, N.; Zhao, X.; Song, Y.; Maharjan, S.; Zhang, J.; Lu, L.; Wang, H.; Yang, B. The crosslink enhanced emission (CEE) in non-conjugated polymer dots: from the photoluminescence mechanism to the cellular uptake mechanism and internalization. *Chem. Commun.* **2014**, *50*, 13845–13848.
- (47) Javed, N.; Cheng, Z.; Zhu, K.; Crichton, R.; Maddali, H.; Hall, G.; Zhang, J.; Li, J.; O'Carroll, D. M. Carbon Dot-like Molecular Nanoparticles, Their Photophysical Properties, and Implications for LEDs. ACS Appl. Nano Mater. 2022, 5, 11741–11751.
- (48) de Boever, R.; Langlois, A.; Li, X.; Claverie, J. P. Graphitic Dots Combining Photophysical Characteristics of Organic Molecular Fluorophores and Inorganic Quantum Dots. *JACS Au* **2021**, *1*, 843–851
- (49) Mary Alex, A.; Kiran, M. D.; Hari, G.; Krishnan, A.; Jayan, J. S.; Saritha, A. Carbon dots: A green synthesis from Lawsonia inermis leaves. *Mater. Today: Proc.* **2020**, *26*, 716–719.
- (50) Si, L.; Shi, Z.; Hou, J.; Miao, C.; Hou, Q.; Xu, Z.; Ai, S. Lignin-Derived Carbon Dot/Cellulose Nanofiber Films for Real-Time Food Freshness Monitoring. *ACS Appl. Nano Mater.* **2022**, *5*, 16620–16632.
- (51) Sun, Z.; Zhou, W.; Luo, J.; Fan, J.; Wu, Z.-c.; Zhu, H.; Huang, J.; Zhang, X. High-efficient and pH-sensitive orange luminescence from silicon-doped carbon dots for information encryption and bio-imaging. *J. Colloid Interface Sci.* **2022**, *607*, 16–23.
- (52) Sun, S.; Jiang, K.; Qian, S.; Wang, Y.; Lin, H. Applying Carbon Dots-Metal Ions Ensembles as a Multichannel Fluorescent Sensor Array: Detection and Discrimination of Phosphate Anions. *Anal. Chem.* **2017**, *89*, 5542–5548.
- (53) Orhan, O.; Haffner-Staton, E.; La Rocca, A.; Fay, M. Characterisation of flame-generated soot and soot-in-oil using electron tomography volume reconstructions and comparison with traditional 2D-TEM measurements. *Tribol. Int.* **2016**, *104*, 272–284.
- (54) Kang, C.; Tao, S.; Yang, F.; Yang, B. Aggregation and luminescence in carbonized polymer dots. *Aggregate* **2022**, 3 (2), No. e169.
- (55) Zhao, X.; Li, J.; Liu, D.; Yang, M.; Wang, W.; Zhu, S.; Yang, B. Self-Enhanced Carbonized Polymer Dots for Selective Visualization of Lysosomes and Real-Time Apoptosis Monitoring. *iScience* **2020**, 23 (4), No. 100982.

- (56) Mao, J.-Y.; Unnikrishnan, B.; Chu, H.-W.; Harroun, S. G.; Chen, Y.-R.; Wu, A.-T.; Chang, H.-T.; Lin, H.-J.; Huang, C.-C. Thermally driven formation of polyphenolic carbonized nanogels with high anticoagulant activity from polysaccharides. *Biomater. Sci.* **2021**, *9*, 4679–4690.
- (57) Elavarasan, S.; Gopalakrishnan, M. Synthesis, structural analysis, theoretical studies of some lawsone derivatives. *Spectrochim. Acta. A* **2014**, 133, 1–6.
- (58) Tandon, V. K.; Yadav, D. B.; Singh, R. V.; Chaturvedi, A. K.; Shukla, P. K. Synthesis and biological evaluation of novel (1)- α -amino acid methyl ester, heteroalkyl, and aryl substituted 1,4-naphthoquinone derivatives as antifungal and antibacterial agents. *Bioorg. Med. Chem. Lett.* **2005**, *15*, 5324–5328.
- (59) Shamsipur, M.; Barati, A.; Taherpour, A. A.; Jamshidi, M. Resolving the Multiple Emission Centers in Carbon Dots: From Fluorophore Molecular States to Aromatic Domain States and Carbon-Core States. *J. Phys. Chem. Lett.* **2018**, *9*, 4189–4198.
- (60) Ananth, S.; Vivek, P.; Arumanayagam, T.; Murugakoothan, P. Natural dye extract of lawsonia inermis seed as photo sensitizer for titanium dioxide based dye sensitized solar cells. *Spectrochim. Acta. A* **2014**, *128*, 420–426.
- (61) Sowmya, S.; Pooja, P.; Ruba, N.; Janarthanan, B.; Nagamani Prabu, A.; Chandrasekaran, J. A study on the fabrication and characterization of dye-sensitized solar cells with Amaranthus red and Lawsonia inermis as sensitizers with maximum absorption of visible light. *J. Mater. Sci. Mater. Electron.* **2020**, *31*, 6027–6035.
- (62) Chanana, G.; Batra, K. Modelling natural dye molecules lawsone and purpurin in different solvents for DSSC applications: a DFT and TD-DFT study. *Molecular Simul.* **2022**, *48*, 760–775.
- (63) Jinchu, I.; Sreekala, C. O.; Sreelatha, K. S. Lawsone metal complex as an effective sensitizer for dye sensitized solar cells. *Mater. Today Proc.* **2020**, *33*, 1356–1360.
- (64) Monroy-Cárdenas, M.; Forero-Doria, O.; Araya-Maturana, R.; Martínez-Cifuentes, M. An Experimental and Theoretical Study of Dye Properties of Thiophenyl Derivatives of 2-Hydroxy-1,4-naphthoquinone (Lawsone). *Materials* **2021**, *14*, 5587.
- (65) S., S.; Pesala, B. Performance Enhancement of Betanin Solar Cells Co-Sensitized with Indigo and Lawsone: A Comparative Study. *ACS Omega* **2019**, *4*, 18023–18034.
- (66) Zimmermann, U.; Malinowski, N.; Burkhardt, A.; Martin, T.P. Metal-coated fullerenes. *Carbon* 1995, 33, 995–1006.
- (67) Hagfeldt, A.; Boschloo, G.; Sun, L.; Kloo, L.; Pettersson, H. Dye-Sensitized Solar Cells. *Chem. Rev.* **2010**, *110*, 6595–6663.
- (68) Bock, C. R.; Connor, J. A.; Gutierrez, A. R.; Meyer, T. J.; Whitten, D. G.; Sullivan, B. P.; Nagle, J. K. Estimation of excited-state redox potentials by electron-transfer quenching. Application of electron-transfer theory to excited-state redox processes. *J. Am. Chem. Soc.* 1979, 101, 4815–4824.